Spray Pyrolyzed TiO₂ Embedded Multi-Layer Front Contact Design for High-Efficiency Perovskite Solar Cells
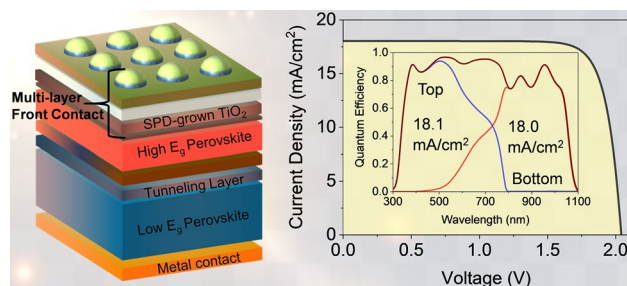
Md. Shahiduzzaman[1,3] ✉, Mohammad Ismail Hossain[2,8], Sem Visal[5], Tetsuya Kaneko[5], Wayesh Qarony[2], Shinjiro Umezu[6], Koji Tomita[4], Satoru Iwamori[3,5], Dietmar Knipp[9], Yuen Hong Tsang[2], Md. Akhtaruzzaman[7] ✉, Jean-Michel Nunzi[1,10], Tetsuya Taima[1], Masao Isomura[4] ✉

HIGHLIGHTS

- Industrially viable bottom-up spray pyrolysis deposition technique was used to prepare the highly compact TiO₂ film, which is a vital element for the multi-layer front contact.

- The optimization of the front contact is presented by fabricating reproducible and efficient perovskite solar cells

- Multi-layer front contact is applied to realize efficient perovskite single-junction and perovskite/perovskite tandem solar cells, where optics and electrical effects of solar cells are studied by optically coupled 3D electromagnetic simulations.

ABSTRACT The photovoltaic performance of perovskite solar cells (PSCs) can be improved by utilizing efficient front contact. However, it has always been a significant challenge for fabricating high-quality, scalable, controllable, and cost-effective front contact. This study proposes a realistic multi-layer front contact design to realize efficient single-junction PSCs and perovskite/perovskite tandem solar cells (TSCs). As a critical part of the front contact, we prepared a highly compact titanium oxide (TiO₂) film by industrially viable Spray Pyrolysis Deposition (SPD), which acts as a potential electron transport layer

(ETL) for the fabrication of PSCs. Optimization and reproducibility of the TiO₂ ETL were discretely investigated while fabricating a set of planar PSCs. As the front contact has a significant influence on the optoelectronic properties of PSCs, hence, we investigated the optics and electrical effects of PSCs by three-dimensional (3D) finite-difference time-domain (FDTD) and finite element method (FEM) rigorous simulations. The investigation allows us to compare experimental results with the outcome from simulations. Furthermore, an optimized single-junction PSC is designed to enhance the energy conversion efficiency (ECE) by > 30% compared to the planar reference PSC. Finally, the study has been progressed to the realization of all-perovskite TSC that can reach the ECE, exceeding 30%. Detailed guidance for the completion of high-performance PSCs is provided.

KEYWORDS Perovskite; Tandem solar cells; Spray pyrolysis deposition; TiO₂ compact layer; Optics and optimization; Electrical characteristic

Md. Shahiduzzaman and Mohammad Ismail Hossain contributed equally to this work

✉ Md. Shahiduzzaman, shahiduzzaman@se.kanazawa-u.ac.jp; Md. Akhtaruzzaman; akhtar@ukm.edu.my; Masao Isomura; isomura@tokai.ac.jp

1 Nanomaterials Research Institute (NanoMaRi), Kanazawa University, Kakuma, Kanazawa 920-1192, Japan

2 Department of Applied Physics and Materials Research Center, The Hong Kong Polytechnic University, Hung Hom, Kowloon, Hong Kong, P. R. China

1 Introduction

Perovskite material systems have attracted considerable research attention to the academic and industrial communities due to their exciting optoelectronic properties, including tunable bandgap, high absorption coefficient, more considerable diffusion length, and low processing costs [1–5]. The energy conversion efficiency (ECE) of single-junction perovskite solar cells (PSCs) has now increased rapidly by more than 25% [6], since Miyasaka and co-workers first reported perovskites as a photo-absorber material with an ECE of 3.8% [3]. Furthermore, the multi-bandgap property of perovskites allows realizing high-efficiency tandem solar cells (TSCs) [5, 7–11], which have a tremendous ability to surpass the Shockley-Queisser (SQ) limit of silicon solar cells [12, 13]. According to the detailed-balance theory, ECE of the TSC may go beyond 45% if the optimum material bandgaps (∼ 1.1 and ∼ 1.73 eV) are selected [9, 12]. However, high-efficiency PSCs reported in literature often suffer from a reproducibility problem, which is one of the significant issues in PSC fabrication and their future commercialization [14]. Typically, the front contact has a significant influence on the electrical and optical properties of a PSC, which needs to be efficient enough so that it can fulfill some fundamental requirements (e.g., improved light incouping, high optical transparency, high lateral conductivity, and low absorption loss) for achieving efficient photon absorption in the solar cell [15]. The front contact with a single layer cannot facility all essential benefits; hence, it requires a multi-layer architecture for efficient PSCs. In a multi-layer front contact, a hole blocking/electron transport layer (ETL) is considered a key element that needs to be compact, smoothly distributed, and pin-hole-free to achieve high ECEs [16–18]. In addition, the qualities of the ETL, such as energy level alignment, charge mobility, morphology, and related interface properties, are prominently valuable for the determination of PSCs with the better photovoltaic performance [15, 19]. Hence, a detailed understanding of the front contact design, deposition techniques, and optoelectronic properties of materials are essential while aiming for high-efficiency PSCs.

The current study preliminary focuses on the selection, preparation, and optimization of the ETL so that the optimized ETL can be utilized to make efficient multi-layer front contact for realizing PSCs with high-efficiency. Until now, a wide variety of metal oxides, such as ZnO, SnO_2, TiO_2, and WO_3, have been investigated as electron transport materials (ETMs) ought to their high electron mobility and enhanced environmental stability [8, 15, 20–22]. Amongst, TiO_2 is considerably popular due to its potential simple deposition, suitable energy level, and tunable electronic properties [23–25]. Furthermore, TiO_2 can produce a smooth film surface to improve charge transfer while maintaining the uniformity [19, 23]. Several deposition methods, such as spin-coating, spray pyrolysis deposition (SPD), atomic layer deposition (ALD), chemical vapor deposition (CVD), sputtering, have been used to prepare TiO_2 compact layer (CL) [18, 19, 23, 26–30]. The current work investigates the preparation of high-quality (compact, uniform, and reproducible) TiO_2 films by the SPD technique so that the film can be used as an ETL for the fabrication of efficient PSCs. The SPD technique is commonly used in industries for a massive area film deposition [31]. The study also focuses on the optimization and reproducibility of the film while fabricating the real devices. Next, the study progressed to the realization of the multi-layer front contact embedded with an optimized TiO_2 CL, so that the efficiency of both single-junction PSCs and perovskite/perovskite TSCs can be maximized. A comparison of the investigated outcome with the theoretical upper limit of PSCs will be provided. The optics and optimization processes are studied by three-dimensional finite-difference time-domain (FDTD) simulations. The electrical characteristics of solar cells are investigated through the finite

[3]   Research Institute of Science and Technology, Tokai University, Kitakaname, Hiratsuka 259-1292, Japan

[4]   Department of Chemistry, School of Science, Tokai University, Kitakaname, Hiratsuka 259-1292, Japan

[5]   Graduate School of Engineering, Tokai University, Kitakaname, Hiratsuka 259-1292, Japan

[6]   Department of Modern Mechanical Engineering, Waseda University, 3-4-1 Okubo, Shinjuku, Tokyo 169-8555, Japan

[7]   Solar Energy Research Institute, The National University of Malaysia, 43600 Bangi, Selangor, Malaysia

[8]   Department of Materials Science and Engineering, City University of Hong Kong, Kowloon, Hong Kong, P. R. China

[9]   Geballe Laboratory for Advanced Materials, Department of Materials Science and Engineering, Stanford University, Stanford, USA

[10] Department of Physics, Engineering Physics and Astronomy, Queens University, Kingston, ON, Canada

element method (FEM) simulations. A fair comparison between experimental results and simulation findings will be provided to validate the numerical approach.

2 Methods

2.1 Materials and Characterization

Lead iodide (PbI_2) and methylammonium iodide (CH_3NH_3I) were purchased from Tokyo Chemical Industry (Tokyo, Japan). Titanium diisopropoxide bis (acetylacetonate; Aldrich, 75 wt%) in isopropanol was bought from the Wako chemical. *N,N*-dimethylformamide (DMF, purity 99.5%) and Dimethyl sulfoxide (DMSO, purity 99.5%) were also purchased from Wako Chemical (Tokyo, Japan). The field emission scanning electron microscopy (FE-SEM; S-4800, Hitachi High-Tech, Tokyo, Japan) was used to analyze the resulting surface morphologies. The ultraviolet–visible near-infrared spectrophotometer (UV–Vis–NIR; V-670, Jasco Corporation, Tokyo, Japan) was used to measure the absorption spectra from the deposited samples. The X-ray diffraction (XRD) patterns of perovskite films were measured using an X-ray diffractometer (D8 Discover, Bruker AXS Co. Ltd, Tokyo, Japan) with an X-ray tube (Cu Kα radiation, $\lambda = 1.5406$ Å). The current density *versus* voltage (*J-V*) characteristics at a scan speed of 0.05 V s^{-1} with forward scan (FS; from −0.1 to 1.2 V) and reverse scan (RS; from 1.2 V to −0.1 V) of the resultant devices was analyzed under simulated (100 mW cm^{-2}, AM1.5, 1 sun intensity) by a solar simulator using a Keithley 2401 digital source meter. The incident photon-to-electron conversion efficiency (IECE) of the resultant devices was tested using a monochromatic xenon arc light system (Bunkoukeiki, SMI-250JA). All the devices were characterized in air, humidity ranging from 40 to 50%, and temperature around 22 °C. The active area of the device was 0.09 cm^2.

2.2 Device Fabrication

The transparent conducting fluorine-doped tin oxide FTO/patterned glass substrates with a sheet resistance of 10 Ω sq^{-1} were cleaned with soap solution, distilled water, acetone, ethyl alcohol, and again distilled water. Subsequently, substrates were further cleaned by UV-ozone treatment for 15 min. Then, a compact TiO$_2$ layer was deposited on the

FTO glass via SPD at 450 °C from a precursor solution of titanium diisopropoxide bis(acetylacetonate) in isopropanol according to the procedure described by Wakamiya et al. [32]. As deposited substrates were left at 450 °C for 30 min in a muffle furnace and let to cool down to room temperature. The perovskite precursor solution (1 M PbI$_2$ and 1 M CH$_3$NH$_3$I in DMF and DMSO mixed solvent) was coated on the resulting substrates. A mixed solution of 1 M PbI$_2$ and 1 M CH$_3$NH$_3$I was dissolved in a mixed solvent of DMF and DMSO (4 V DMF: 1 V DMSO), followed by at 60 °C for 1 h. The perovskite film was prepared by spin-coating the precursor solution at 6000 rpm for 60 s with dripping 500 μL of chlorobenzene just 8 s after the spin-coating started. The precursor coated substrates were then annealed at 100 °C on a hot plate for 1 h to crystallize perovskite in a glove box under an inert environment. We tuned the thickness of TiO$_2$ CL by changing the concentration (0.15, 0.20, 0.25, 0.30, 0.35, and 0.40 M) of TiO$_2$ solution. The champion cell has a TiO$_2$ thickness of 70 nm with the precursor solution concentration of 0.35 M. The thickness of the perovskite absorber was measured to be approx. 300 nm. It is noted that the Perovskite layer only contributes to quantum efficiency (*QE*) and short-circuit current density (*J$_{SC}$*). The detailed hole transport layer (HTL) precursor solution preparation is reported elsewhere [32]. Deposited Spiro-OMeTAD HTL has a thickness of 250 nm. Finally, 100-nm-thick gold (Au) electrodes were deposited on top of the HTL layer to complete the device fabrication.

2.3 Coupled Opto-electrical Simulation Method

The Finite-difference time-domain (FDTD) approach was carried out to investigate the optical wave propagation in single-junction PSCs and perovskite/perovskite TSCs in three-dimension (3D), where precise electromagnetic calculations are solved by Maxwell's equations. The FDTD is one of the most suitable techniques for examining the optics of several optoelectronic devices due to its accurate estimation and broadband frequency coverage. Experimentally realized complex refractive indices were used as input parameters for the optical simulations, which are provided in Fig. S15. Most optical constants were determined from the ellipsometry measurement of deposited films; however, the refractive index and extinction coefficient of MASnPbI$_3$ and SnO$_2$ materials were adapted from the literature [33,

34]. A circularly polarized incident plane wave was considered as a source with the standard AM 1.5G solar spectrum, which has an amplitude of 1000 V m^{-1}. The source was placed in the air that propagates to the solar cell structure from front contact to the back contact. The monochromatic source wavelengths were selected based on the bandgap of the absorber materials. In the current study, optical simulations were carried from 300 to 800 nm for single-junction PSCs, and 300 to 1100 nm was chosen for perovskite/perovskite TSCs. Furthermore, necessary boundary conditions were applied to the simulation region, where the perfect matched layer (PML) boundary condition (BC) was selected for the z-directional outgoing waves so that unwanted reflections can be evaded. In the x- and y- direction, periodic BCs were applied so that periodicity can occur throughout the solar cell structure. The convergence test was performed to attain the accurate mesh size, where the dimension of mesh grids was 5 nm in all cases. Moreover, the layer thickness optimization was carried out by the particle swarm optimization (PSO) embedded with the FDTD method, which allows finding the optimum parameter so that photon absorption in the perovskite layer is maximized, and optical losses are minimized. The PSO algorithm is even much effective while studying a complex geometrical structure. By considering the valid assumption, where each incident photon generates an electron–hole pair (EHP) if the bandgap of the perovskite absorber is lower than the incident photon energy. A further detail on how to calculate total generation rate, power densities, QE, J_{SC}, and V_{OC} are provided in Sect. S2.

To estimate the realistic photovoltaic performance, electrical parameters play an additional critical role. However, optical simulations do not allow determining electrical parameters of the solar cell. Therefore, as a mandatory part, electrical simulations were performed thoroughly of investigated solar cells by the finite element method (FEM), which allows determining the current–voltage (*J-V*) characteristic curve of the solar cell. A set of necessary electronic parameters of materials was used for the calculation, which were adapted from the literature and summarized in Table S5 [35–40]. A more detailed description of the electrical simulation is provided in Section S3 and literatures [11, 37]. Such an advanced numerical approach with the combination of optical and electrical simulations provides excellent agreement with the experiments [36, 37, 41], as experimentally realized material properties were used in the simulation environment.

3 Results and Discussion

3.1 Planar Solar Cell Design and Film Preparation

In the first step of this study, a planar PSC was investigated. Approximately 300-nm-thick methylammonium lead iodide (MAPbI$_3$) perovskite with a bandgap of ~1.5 eV is placed between charge transport layers to form the n-i-p junction. A schematic diagram of the planar PSC is depicted in Fig. 1a, and corresponding energy levels are shown in Fig. 1b [42, 43].

As TiO$_2$-CL is one of the key elements for PSCs; hence, the TiO$_2$ film's optimization has been carried out to determine the optimum ETL thickness. The TiO$_2$ film was prepared on the FTO substrate, where the TiO$_2$ precursor solution was tuned from 0.15 to 0.40 M. It has been discovered that the TiO$_2$-CL with a precursor concentration of 0.35 M, with a thickness of ~70 nm, only exhibits excellent uniformity and smooth surface morphology, as shown in Fig. 1c. Fig. 1d illustrates the top-view SEM image of MAPbI$_3$ film deposited on the TiO$_2$/FTO, which shows a standard surface morphology with densely packed perovskite crystals where grain size varies approximately from 200 to 500 nm. Figure S1a shows the UV–vis absorption spectrum for the wavelength range of 300–820 nm. The absorbance goes zero while reaching the wavelength of 800 nm, which proves the perfection of perovskite material properties. The XRD patterns are illustrated in Fig. S1b, where diffraction peaks are detected at 2θ angles of 14.1°, 28.7°, 31.8°, and 40.74° in TiO$_2$ CL/MAPbI$_3$ film, which corresponds to (110), (220), (310), and (224) crystal planes, respectively. There was no peak from PbI$_2$ at 12.6°, implying that the complete transformation of PbI$_2$.

3.2 Reproducibility of Single-junction Planar Perovskite Solar Cells

The effect of the TiO$_2$ hole blocking layer on the photovoltaic performance of single-junction planar PSCs is studied. A PSCs group with the structure FTO/TiO$_2$ CL/MAPbI$_3$/Spiro-OMeTAD/Au was fabricated, where the device performance was analyzed under one sun (AM 1.5G, 100 mW cm^{-2}) conditions. The concentration of TiO$_2$ precursor solution was varied from 0.15 to 0.40 M while fabricating
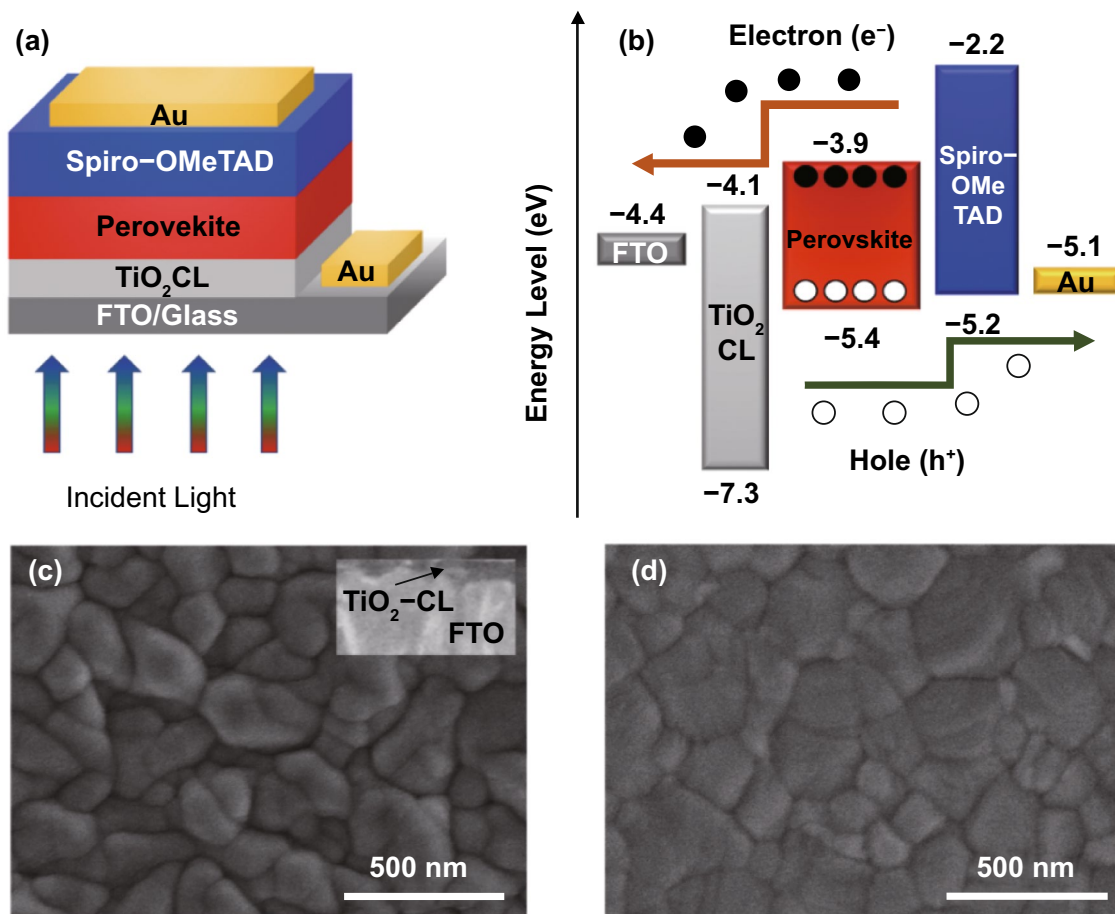
Fig. 1 **a** Schematic diagram and **b** corresponding energy levels of the investigated single-junction planar perovskite solar cell. Top-view SEM micrographs of **c** spray pyrolysis deposited TiO₂ compact layer (the inset shows the cross-sectional view of the TiO₂), and **d** perovskite film deposited on TiO₂-CL/FTO substrate. The TiO₂ precursor solution has a concentration of 0.35 M and a thickness of 70 nm

the device. A cross-sectional SEM image of the fabricated planar PSC is depicted in Fig. 2a, where a TiO₂ CL is placed between the MAPbI₃ absorber and FTO glass substrate. The typical current–voltage (*J-V*) characteristic curves with the reverse scan (RS) of the fabricated PSCs against various concentrations of TiO₂ precursor solution are presented in Fig. 2b. The *J-V* curves of fabricated PSCs with forward scan (FS) and reverse scan (RS) are given in the Supporting Information (Fig. S2). A wide discrepancy of *J-V* curves is observed while varying the concentration of the TiO₂ precursor solution. The photovoltaic performance of fabricated devices with different TiO₂ precursor solution concentrations was compared using photovoltaic parameters extracted from *J-V* curves, as shown in the supporting information (Fig. S3). A variation of the TiO₂ precursor solution concentration leads to J_{SC}, V_{OC}, and *FF*

from 13.3 to 21.3 mA cm^{-2}, 0.99 to 1.08 V, and 65.8% to 72%, respectively, with the RS.

On the other hand, J_{SC}, V_{OC}, and *FF* ranged from 15.07 to 21.4 mA cm^{-2}, 0.99 to 1.075 V, and 50.4% to 69%, respectively, with the FS. J_{SC} and V_{OC} are only maximized in the case of 0.35 M, where the TiO₂ CL has a 70-nm thickness, resulting in improved ECE. As compared to others, the 0.35 M condition exhibits a low hysteresis problem, allowing it to reach an ECE of 16.55%. In addition to that, light soaking and moisture stability tests of fabricated planar PSCs are provided in Fig. S4. More detailed information on such devices' stability can be found from our previously published works in the literature [26, 44]. Up to our knowledge, this is the uppermost ECE, which is experimentally realized from the basic planar PSC with the incorporation of only the SPD-grown TiO₂ CL as the ETL. Further optimization of
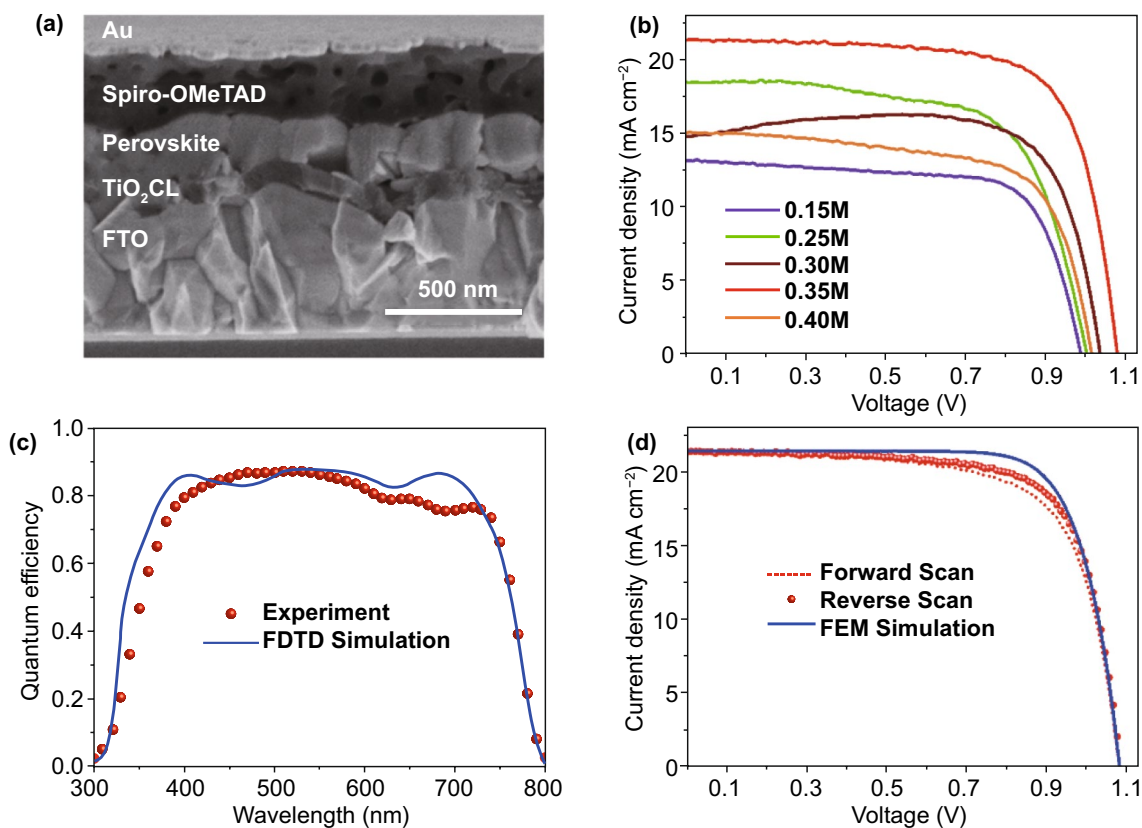
Fig. 2 **a** Cross-sectional FESEM image of the fabricated champion planar perovskite solar cell. **b** Current–voltage (*J-V*) curves with the reverse scan (RS) for the fabricated planar PSCs with different TiO$_2$ precursor solution concentration. **c** Comparison of quantum efficiencies between experiment and FDTD optical simulation. **d** Forward scan (FS) and reverse scan (RS) *J-V* curves of the fabricated best performing PSC along with the *J-V* curve realized from the FEM electrical simulation

planar PSCs has been carried by utilizing 3D-FDTD optical simulation integrated with particle swarm optimization (PSO) algorithm to determine the thickness of the TiO$_2$ CL. A detailed description of the optical simulation is provided in the methods section. It has been found that the thickness of a TiO$_2$ CL in PSCs has a significant impact on the optics of the solar cell. The TiO$_2$ CL thickness dependent QEs and parasitic absorptions are presented in Fig. S5. The optical simulation findings provided an excellent agreement with the experimentally realized outcome, where the QE of a planar PSC is maximized by reducing parasitic loss only when the TiO$_2$ CL has a thickness of 70 nm. A comparison of experimentally realized and simulated QEs is shown in Fig. 2c. The TiO$_2$ ETL absorbs a major portion of incident photons in the UV range; however, photons within the visible wavelength range (400–700 nm) are primarily absorbed by the perovskite absorber layer. Noticeably, both QEs exhibit almost identical characteristics after 750 nm

wavelength, which shows the work's validity. Such optical phenomena in the solar cell can be further verified by their calculated power density and electrical distribution profiles given in Figs. S6, S7. By looking at power densities and electric distributions, the QE is thought to be understood only from constructive and destructive waves due to forward and backward wave propagations. No scattering or diffraction is noticeable in the planar configuration of the PSC, which also suggests that a significant portion of incident light is lost only due to high reflections. Such reflections can be minimized, and photon absorption can be enhanced in the PSC using multi-layer photonic structures [45]. The PSC integrated with a front photonic structure can further reduce the UV radiation, improving device stability [25, 45].

However, optical simulations do not provide electrical parameter values for the solar cell; hence, FEM simulations were adapted to investigate the electrical effects of the solar cell by allowing a *J-V* characteristic curve. A

wide range of essential electronic properties of materials was used for the FEM calculations. More details on the FEM electrical simulations are provided in the Methods section. A comparison of *J-V* characteristic curves between experiment and simulation is provided in Fig. 2d for the best performing device. The *J-V* curves show a comparable characteristic by validating the experimental data with numerical simulations. Corresponding extracted photovoltaic parameters from the *J-V* curves are summarized in Table 1.

The J_{SC} and the V_{OC} are almost equivalent in each case; however, the fabricated device's ECE (16.55%) is limited due to a slight reduction of the *FF* compared to the simulated device (ECE ~ 17.47%). It is assumed that the imperfection of interfaces between perovskite and contact layers may lead to a lower *FF* in the real fabrication.

As the next step of this study, we started investigating PSC reproducibility by considering 13 fabricated devices in each group (total 6 groups) to attain an optimized planar PSC design for future investigations. As before, the concentration of the TiO$_2$ precursor solution was ranged from 0.15 to 0.40 M while fabricating the PSC device. The photovoltaic parameters were extracted from each *J-V* curve. The average values of V_{OC}, J_{SC}, *FF*, and ECE of resultant fabricated PSCs as a function of TiO$_2$ precursor solution concentration are illustrated in Fig. 3a-d. Error bars indicate plus or minus the standard deviation from the mean value.

As anticipated, PSCs with the 0.35 M TiO$_2$ precursor solution concentration demonstrated a superior performance as compared to other cases (0.15, 0.20, 0.25,
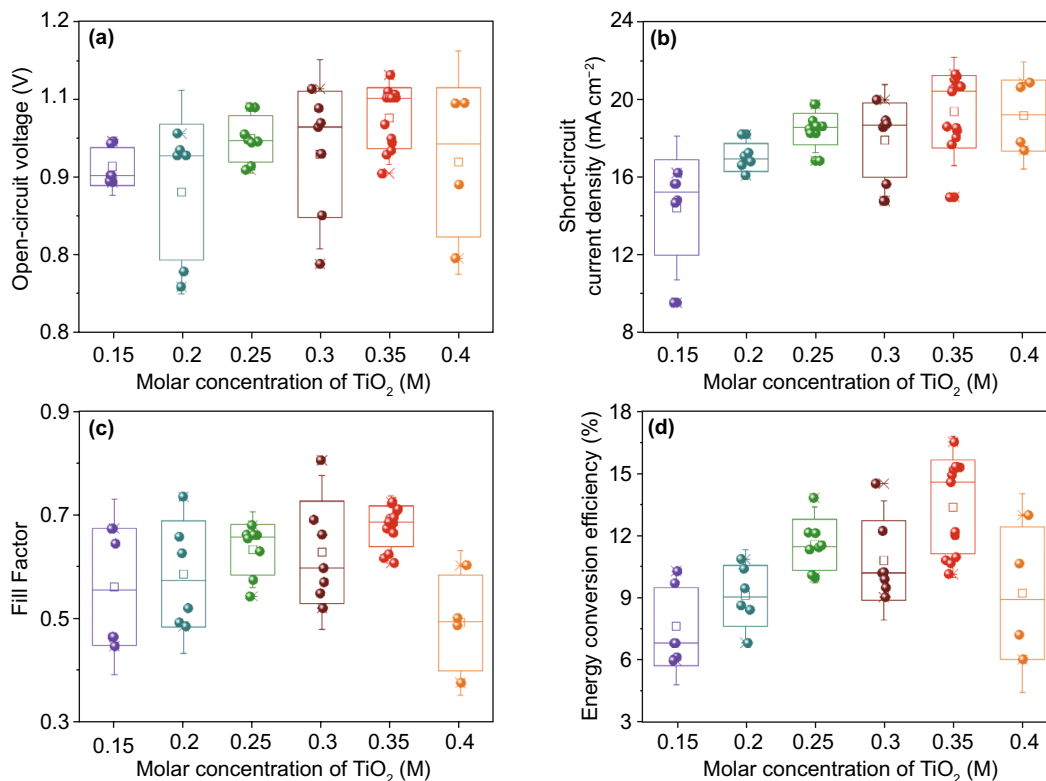
Table 1 A comparison between experiment and simulation for photovoltaic performance parameters extracted from *J-V* characteristics of planar PSCs, as shown in Fig. 2d

Method	Performance Parameters			
	V_{oc} (V)	J_{sc} (mA cm^{-2})	FF (%)	ECE (%)
Experiment (FS)	1.07	21.48	65	15.16
Experiment (RS)	1.07	21.30	72	16.55
FEM Simulation	1.07	21.40	76	17.47

Fig. 3 Average values of **a** open-circuit voltage (V_{OC}), **b** short-circuit current density (J_{SC}), **c** fill-factor (*FF*), and **d** energy conversion efficiency (*ECE*) obtained from resultant 13 fabricated devices in each group while varying the molar concentration of the TiO$_2$ precursor solution from 0.15 to 0.40 M

0.30, and 0.40 M). The 0.35 M case yield better reproducibility and average V_{OC}, J_{SC}, FF, ECE of 1.02 ± 0.06 V, 19.37 ± 1.9 mA cm^{-2}, $67 \pm 5\%$, $13.5 \pm 3.05\%$, respectively. The statistics of PSC performances of 13 devices are summarized in Table S1, where results can be attributed to the enhanced morphology and crystallinity of perovskite films using optimized TiO$_2$ precursor solution concentration. The best-performance PSC has an optimized TiO$_2$ ETL thickness of approx. 70 nm, which shows a maximum ECE of 16.55% with a J_{SC} of 21.30 mA cm^{-2}, a V_{OC} of 1.07 V, and a FF of 72%. However, as the photovoltaic performance of planar PSCs yet limited due to higher optical losses, next part of this study focuses on the efficient photon management so that light incoupling and/or light trapping in the solar cell can be improved.

3.3 Photon Management in Perovskite Solar Cells

The fabricated basic planar PSC with the TiO$_2$-CL ETL has the potential to reach high ECE. However, the present device design does not allow adequate photon absorptions in the perovskite absorber because of higher optical losses that prevents the realization of efficient PSCs. Efficient photon management allows realizing PSCs with high ECEs with the improved light incoupling and/or light trapping. By texturing the solar cell interfaces, improved light incoupling and light trapping in the solar cell can be achieved; however, this negatively influences the electrical parameters, such as V_{OC} and FF. Efficient solar cell mostly requires flat interfaces between absorbers and contacts to ensure better electrical parameters. Nevertheless, a single compact layer of TiO$_2$ is not enough for efficient electron extraction/hole blocking from the perovskite absorber, which also suffers from severe recombination problems at the perovskite/front contact interface that limits the electrical performance of the solar cell. Hence, incorporation of mesoporous TiO$_2$ (mp-TiO$_2$) could be one of the potential solutions which contributes to the effective electron transportation. The mp-TiO$_2$ nanoparticles further allow reducing the recombination of carriers. In addition to that, the mp-TiO$_2$ contributes to the realization of dense and pinhole-free perovskite film, resulting in the higher crystallinity. Subsequently, the electrical parameter (V_{OC}, FF) values are improved. The mp-TiO$_2$ additionally contributes

to the enhancement of photon absorptions through the photon scattering in the active layer, leading to achieve high J_{SC} and ECE.

In the optimized device design, we have used a multilayer front contact by the use of metal oxides, which has a comparable refractive index ($2.2 \sim 2.5$) with the perovskite absorber. Thus, the layer stack consisting of front contact and perovskite absorber can be treated as a single block, which leads to reduce reflections at the front contact/perovskite interface and helps to maximize QE and J_{SC} [46, 47]. Consequently, the optical design of the solar cell is simplified, and by only focusing the light incoupling, photon absorptions can be improved, and reflections can be minimized. Light incoupling can be further enhanced by using a textured anti-reflection (ARC) layer, which has a refractive index of around ~ 1.4. Such an ARC layer acts as a refractive index gradient while incident light propagates from air to the solar cell. In this study, efficient photon management was achieved by improving light incoupling and light trapping. The light incoupling was attained by the utilization of a distinctive periodic semi-sphere shaped MgF$_2$ layer, which facilitates like a broadband ARC so that light incoupling can be significantly improved by minimizing reflections. A part of light trapping was achieved by introducing mp-TiO$_2$ nanoparticles. A schematic diagram of the proposed PSC structure by incorporating a multi-layer front contact layer is depicted in Fig. 4a. Figure 4b shows the graphical representation of the MgF$_2$ ARC layer, which was deposited on top of the solar cell. The semi-sphere nanostructure can be prepared by casting an MgF$_2$ film on a crystalline silicon master, which is patterned by silicon semiconductor processing [48]. The ARC is characterized by a circular base arranged nanostructure in a square grid, which can provide almost ideal light incoupling in the solar cell. The diameter of the nanostructure is assumed to be the same as the diameter of mp-TiO$_2$ nanoparticle; in this study, it was 100 nm. We have integrated the ARC nanostructure in a PSC, as shown in Fig. 4a, where all solar cell interfaces are assumed to be flat. Such ARC nanostructure and mp-TiO$_2$ nanoparticle allow realizing an improved photon absorption in the absorber layer, which can be seen from the QE plot illustrated in Fig. 4c.

In addition to this, the QE of the investigated planar PSC is included in Fig. 4c. A further comparison of QEs, J_{SC}s, and reflection losses of PSCs without ARC, with a flat ARC, and with a nanostructured ARC is provided in Fig. 5. It has
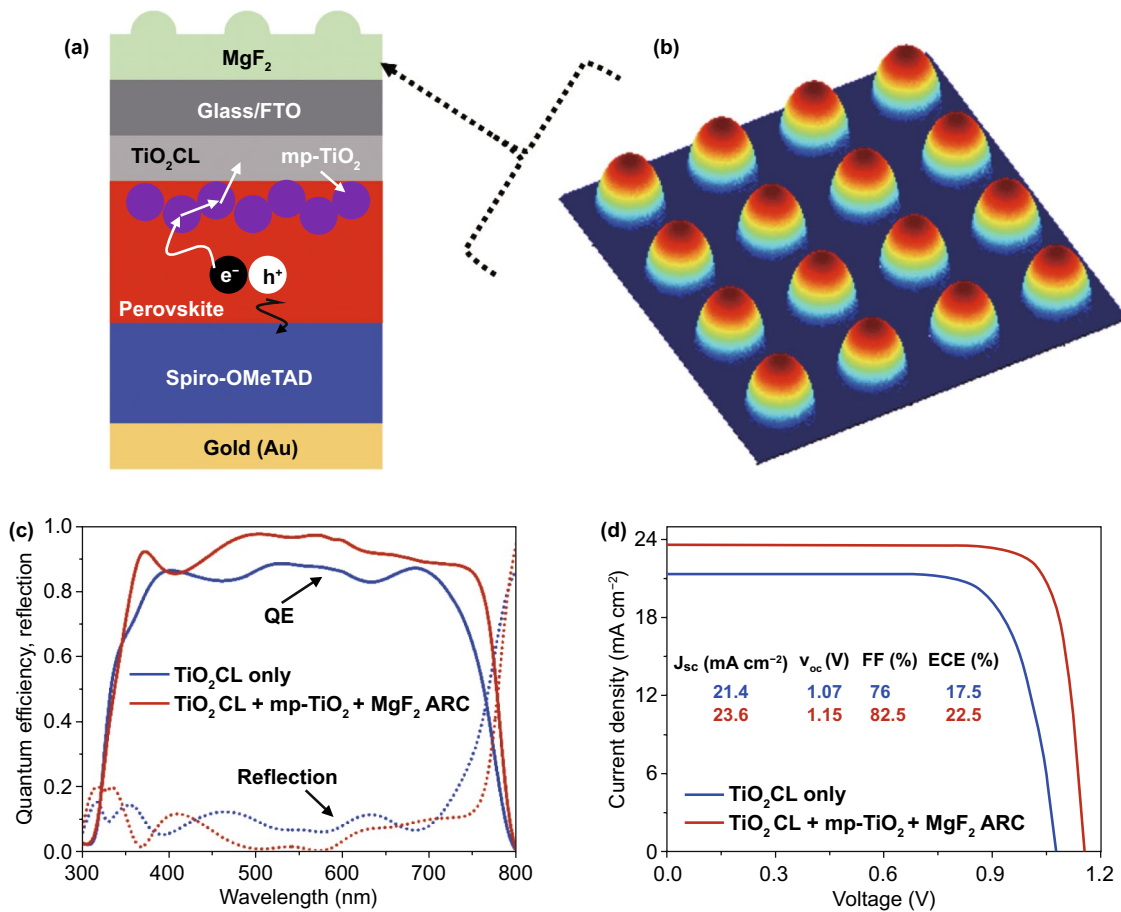
Fig. 4 **a** Schematic diagram of the optimized single-junction perovskite solar cell. **b** Graphical representation of the nanostructured MgF$_2$ ARC layer. A comparison of **c** quantum efficiencies and corresponding reflections, and **d** *J-V* characteristic curves between optimized PSC (MgF$_2$ ARC/FTO/TiO$_2$/mp-TiO$_2$/MAPbI$_3$/Spiro/Au) and planar reference PSC (FTO/TiO$_2$/MAPbI$_3$/Spiro/Au)

been observed that only the incorporation mp-TiO$_2$ nanoparticles is not sufficient to improve the photon absorption in the perovskite layer, somewhat decreasing the *QE* and J_{SC} compared to the reference planar PSC is due to higher optical losses. A significant enhancement in the *QE* is realized only from the optimized structure due to reducing the optical losses. The considerable portion of optical losses is diminished owing to the minimum reflection losses.

A comparison of *QE*s and reflection losses between optimized and other structures are illustrated in Figs. 4c and 5d, e. Throughout the spectrum, the *QE* of the optimized PSC is improved compared to the planar reference PSC. The *QE* is maximized when the front ARC provides efficient light incoupling and $2 \times d \geq t_p$, where d is the absorber thickness, and t_p is the penetration depth of the absorber. On the other hand, if $t_p \geq 2 \times d$, *QE* is maximized due to light trapping. In

this case, a 300-nm-thick perovskite absorber layer was considered in the solar cell structure. Hence, the *QE* enhancement for the short wavelengths up to 660 nm, mostly because of almost perfect light incoupling, whereas at wavelength over 660 nm, *QE* improvement is found due to enhanced light scattering and trapping of the incident light. At 500 nm, the *QE* of the optimized PSC reaches a peak (> 95%), which leads to a corresponding reflection of almost 0. Moreover, a reduced *QE* is observed between 370 to 470 nm, wavelength range, which is due to unwanted reflections at the front of the solar cell. However, the *QE* drops for the longer wavelengths due to non-radiative optical losses caused by back contact. Such optical phenomena can be further appropriately understood by power densities and electric field distributions. Figures S8 and S9 show power density and electric field distribution profiles of the optimized single-junction
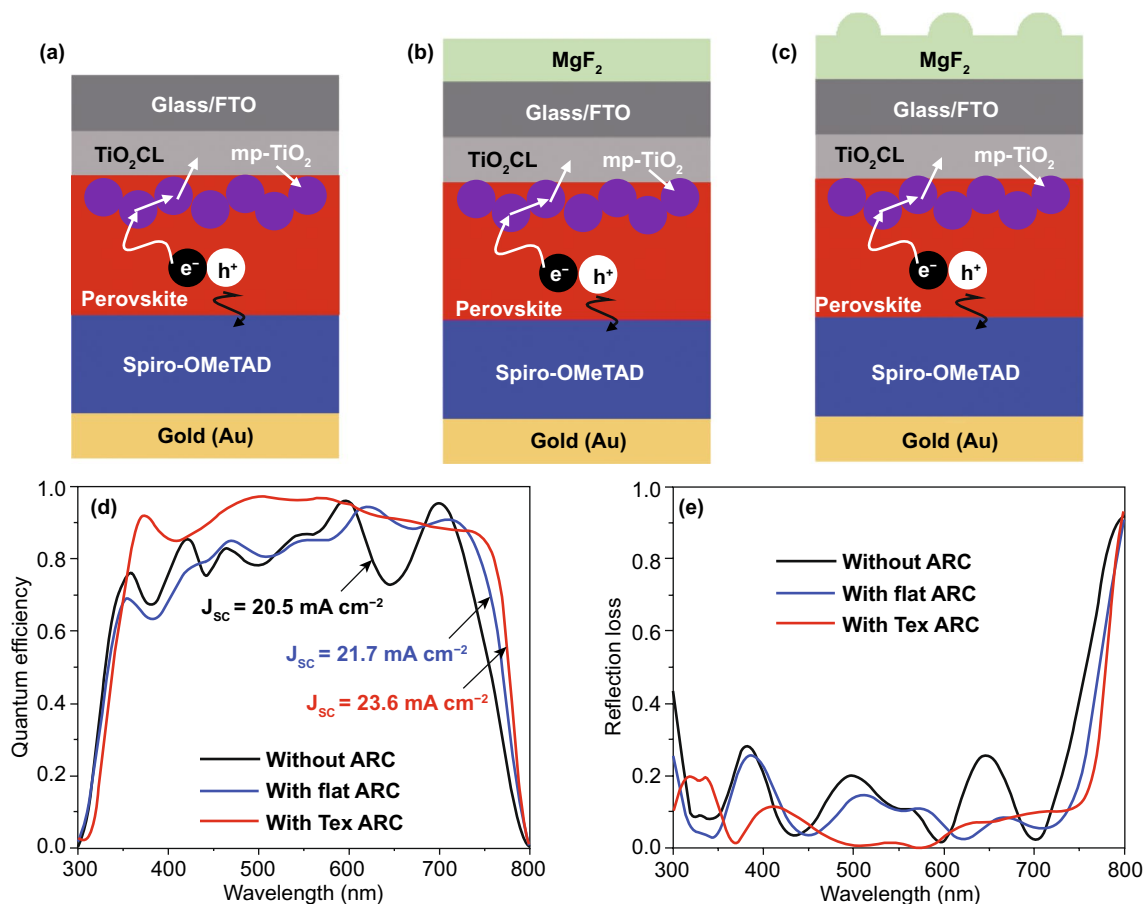
Fig. 5 Schematic diagram of the single-junction perovskite solar cell (PSC) **a** without MgF$_2$ ARC layer, **b** with a flat MgF$_2$ ARC layer, and **c** with a textured MgF$_2$ ARC layer. A comparison of **d** quantum efficiencies (*QE*s) and Short-circuit current densities (*J*$_{SC}$s), and **e** corresponding reflection losses. The perovskite absorber has a thickness of 300 nm

PSC under for an incident wavelength ranging from 300 to 800 nm. It is clearly observed that how the ARC layer contributes to the enhanced light incoupling, and the mp-TiO$_2$ nanoparticles provide photon absorption enhancement through the scattering of the incident light, leading to the formation of a standing wave in the solar cell. Thus, it is confirmed that both nanostructured ARC and mp-TiO$_2$ exhibit almost perfect light incoupling and light trapping, which leads to higher *QE* and greater *J*$_{SC}$ in the simulated spectral range. In comparison to the reference planar PSC, the *J*$_{SC}$ of the optimized PSC is increased from 21.4 to 23.6 mA cm^{-2} because of enhanced photon absorption and minimized optical losses. Such heightening in the light generation additionally also improves the electrical performance parameters of the solar cell. Fig. 4d shows the comparison of investigated J-V characteristics between reference planar and optimized single-junction PSCs. Corresponding extracted photovoltaic performance parameters are listed in Table 2.

Table 2 A comparison of photovoltaic performance parameters of single-junction PSCs extracted from *J-V* characteristic curves

Structure type	Performance Parameters			
	V_{oc} (V)	J_{sc} (mA cm^{-2})	FF (%)	ECE (%)
FTO/**TiO$_2$ CL** /MAPbI$_3$/Spiro/Au	1.07	21.4	76	17.47
MgF$_2$/FTO / **TiO$_2$ CL/ mp-TiO$_2$**/ MAPbI$_3$/Spiro/ Au	1.15	23.6	82.5	22.5

A noticeable improvement of the photovoltaic parameters was found in the case of the optimized PSC, where the V_{OC} and *FF* were improved by 7.5% and 8.6%, respectively, as compared to the reference planar PSC, leading to the enhancement of ECE from 17.47% to 22.5%. As compared to the fabricated planar PSC, the ECE of optimized PSC is improved by ~ 36%. Besides, the influence of electronic parameters, mainly, dopant concentrations on the solar cell performance is provided in Fig. S10 and Tables S2-S4. Since the optimized multi-layer front contact has the potential for realizing high-efficiency single-junction PSCs, the study has been progressed to the investigation of a Perovskite/perovskite TSC for realizing high photovoltaic performance. A detailed guideline for achieving efficient Perovskite/perovskite TSCs is provided in the following section.

3.4 Realization of High-efficiency Perovskite/Perovskite Tandem Solar Cells

In general, the design of efficient TSC is challenging because the current from the top to bottom cell in the TSC must be matched under short-circuit current conditions. Furthermore, the bandgap of the bottom cell absorber in a TSC has to be low so that a high J_{SC} can be reached, which can further contribute to maximizing the matched J_{SC} and ECE of the TSC. Hence, in this study, the investigation originated from the optimization of narrow bandgap single-junction PSCs. The upper limit of the J_{SC} of the perovskite/perovskite TSC can be predicted from the bottom cell J_{SC}, which is 50% of the bottom cell J_{SC}. It is assumed that the low bandgap perovskite can exhibit high J_{SC}, where several studies reported remarkable ways to lower the bandgap by using the Pb/Sn binary perovskite (MAPb1_{-x}Sn$_x$I$_3$) alloys [49–51].

In this study, we propose the use of MASnPbI$_3$ perovskite (E_g ~ 1.16 eV) absorber, which is sandwiched between PCBM and NiO charge transporting layers. NiO provides excellent chemical stability with a suitable work function, exhibiting a higher V_{OC} of the PSC [52]. The absorber thickness plays an essential role in maximizing *QE* and J_{SC} as only photon absorptions in the absorber contribute to the J_{SC} of the solar cell. Thus, to optimize the bottom PSC, the thickness of the absorber layer was varied from 400 to 1000 nm by maintaining the diffusion length. Solar cell with such a low bandgap perovskite allows attaining broadband photon absorptions ranging from 300 to 1100 nm

wavelength region. *QEs* of different thickness of perovskite absorber of the bottom PSC are provided in the supporting information (Fig. S11a), where corresponding J_{SC} ranges from 29.6 to 33 mA cm^{-2} as shown in Fig. S11b in the Supporting Information. It is seen that increasing the absorber thickness leads to enhanced J_{SC}; however, no further improvement has been found after 800 nm, the J_{SC} is saturated. Typically, the bottom part of the perovskite/perovskite TSC gives a high J_{SC} by exhibiting a low V_{OC}. In contrast, the top cell is responsible for enabling high V_{OC} with a suitable J_{SC}. Hence, it is imperative to select an appropriate top cell for efficient TSC. In this study, we used the previously investigated MAPbI$_3$ perovskite absorber as a top cell. By the combination of both top cell and bottom cell in a serial connection, a two-terminal (2 T) perovskite/perovskite TSC was realized, where undoped SnO$_2$ is used a tunneling and interconnecting layer. The SnO$_2$ layer facilitates efficient charge transportations, which can improve the J_{SC} and ECE of the solar cell. In TSC, the photons with high energies are absorbed by the top cell as passes low energy photons so that it can be absorbed by the bottom cell. The phenomena can be seen by the generation contour plots, as illustrated in Fig. 6, where maximum electron–hole pairs are generated in the lower bandgap materials in the solar cell structure. However, a proper realization of the matching current of the TSC is demanding while a top cell is deposited on top of a bottom cell, which needs an advanced optimization technique, including precise mesh, high-level computing, realistic design. The optimization should give an appropriate subcell thickness estimation so that the ECE is not limited by the mismatching issue. In this study, a large number of subcell combinations were selected to investigate *QEs* and J_{SC}s under matching conditions. The optimization process and optics were studied by using particle swarm optimization (PSO) algorithm with 3D-FDTD optical simulations. The top cell thickness was ranging from 150 to 300 nm, while the bottom cell thickness was changing from 400 to 1000 nm. For each combination, matching J_{SC} of the perovskite/perovskite TSC is evaluated, where the contour plot, as illustrated in the supporting information (Fig. S12), demonstrates the J_{SC}s for every possible combination of top and bottom cells. The matched J_{SC} is maximized while the subcell thicknesses are optimum. Findings in optical simulations reveal the upper limit of the J_{SC} (~ 18 mA cm^{-2}) under the matching condition. The maximum matched J_{SC} is attained for the top and bottom cell absorber thickness combination of
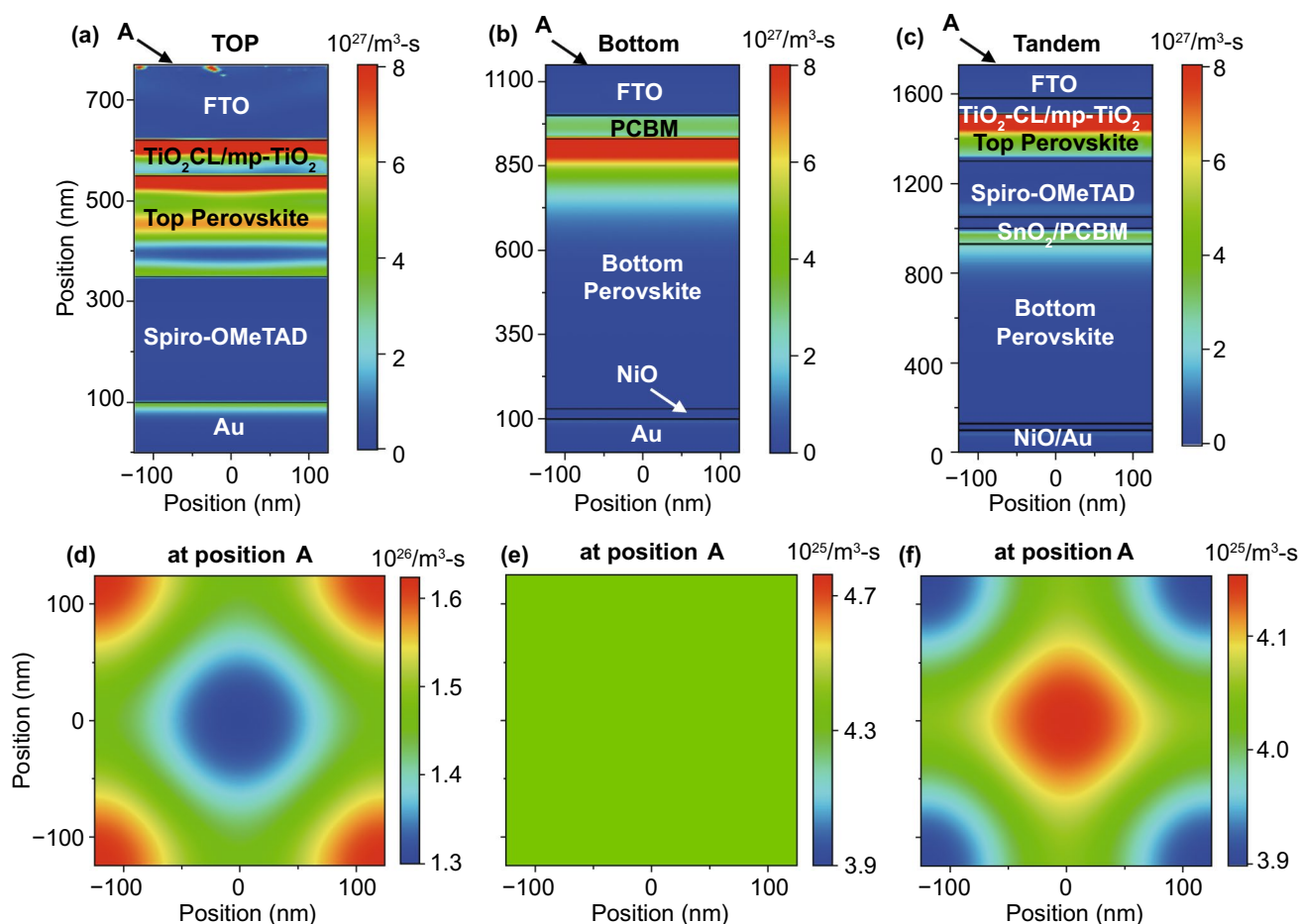
Fig. 6 Total generation rate of **a** single-junction top perovskite (wide E_g) solar cell, **b** single-junction bottom perovskite (narrow E_g) solar cell, and **c** perovskite/perovskite tandem solar cell. **d-f** Corresponding top-view of the generation rate. The top perovskite absorber has a thickness of 210 nm, and the bottom perovskite absorber has a thickness of 800 nm

210 and 800 nm, respectively. A schematic cross-section of the Perovskite/perovskite TSC under matching short-circuit current condition is depicted in Fig. 7a, and corresponding power density profiles under the monochromatic wavelength of 400, 550, 730, and 950 nm are presented in Fig. 7b-e. For short wavelengths (< 400 nm), most photons are absorbed by the front contact /top perovskite interface, while a fraction of the light propagates to the bulk of the perovskite absorber. The increase of wavelength (550 nm) leads to improved photon absorptions in the top absorber, and a certain portion of photons passes to the bottom cell. At 730 nm, photons are equally absorbed by both top and bottom cells, where absorption losses are pronounced in the contacts for further increase in wavelength, leading to a significant improvement of photon absorption in the bottom cell.

In contrast, almost zero absorptions appear in the top cell. Such optical phenomena and absorption mechanisms are further confirmed by the QE plots. Fig. 7f shows the QE of the best performing perovskite/perovskite TSC, which exhibits a matched J_{SC} of 18 mA cm^{-2}. QE plot approves that photons in the shorter wavelengths mostly absorbed by the top cell, while the bottom cell absorbs most photons in the longer wavelengths. This is due to the optimum selection of the materials with suitable bandgaps. At 730 nm, both subcells work at their maximum power point; hence both top and bottom PSCs exhibit equal QE of ~45%. It is assumed that such a high J_{SC} is realized due to the efficient light incoupling and/or light trapping, which is mostly provided by the TiO$_2$ ETL and front nanostructured ARC layer. The parasitic absorptions in the front are very low (< 1 mA cm^{-2});

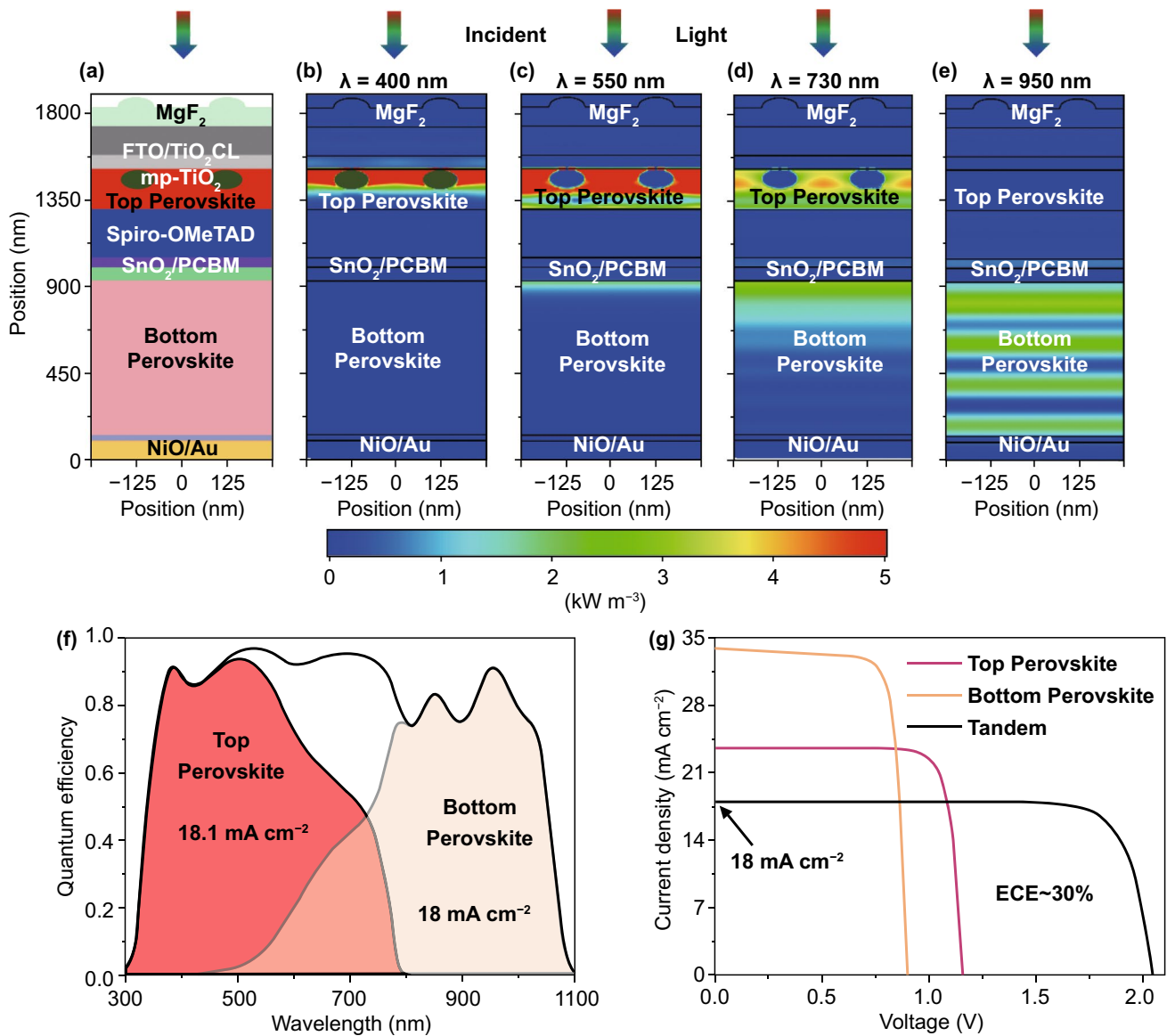**Fig. 7** **a** Schematic cross-section of the optimized perovskite/perovskite tandem solar cell. Corresponding power density profile for an incident wavelength of **b** 400 nm, **c** 550 nm, **d** 730 nm, and **e** 950 nm. **f** Quantum efficiency and **g** current–voltage characteristic curves of the best-investigated perovskite/perovskite tandem solar cells under matching short-circuit current condition, where top perovskite and bottom perovskite has a thickness of 210 and 800 nm, respectively.

however, yet a significant portion of incident lights do not absorb in the solar cell due to higher reflections (~10%).

The optics of the investigated perovskite/perovskite TSC under matching condition is also supported by the electric field distribution profiles for an incident wavelength of 400, 550, 730, and 950 nm, as provided in Fig. S13. Until now, we have focused only on the optics of solar cells so that a maximum matched J_{SC} can be achieved. However, electrical effects are equally essential for determining realistic ECE of

the investigated perovskite/perovskite TSC, which cannot be determined by only optical simulations. Hence, FEM calculations were used for electrical simulations of single-junction subcells and complete TSCs. Here, electron–hole pair (EHP) generations from optical simulations were used as optical input for electrical simulations. A detailed description of the TSC simulation is provided in the Methods section.

Generation rates for top single-junction PSC bottom single-junction PSC, and perovskite/perovskite are

illustrated in Fig. 5a-c. As expected, a high rate of EHP generation occurred in the active layers, which are due to low material bandgaps as compared to other (contact) layers. The generation of photons decreases from top to bottom in the active layer; therefore, the generation rate is comparatively higher close to the surface. Simulations allow providing *J-V* characteristic curves of investigated solar cells, where the photovoltaic performance parameters can be extracted. The *J-V* characteristic curves of investigated individual subcells and complete TSC are shown in Fig. 7g and extracted photovoltaic parameters are listed in Table 3. The investigated single-junction top PSC exhibits an ECE of 22.7% with a J_{SC} of 23.6 mA cm^{-2}, a V_{OC} of 1.15 V, and a FF of 83.5%, whereas the bottom PSC provides an ECE of 24.4% with a J_{SC} of 34 mA cm^{-2}, a V_{OC} of 0.89 V, and a FF of 80.5%. By combining both single-junction PSCs in a TSC structure, the ECE is raised to 30% with a matched J_{SC} of 18 mA cm^{-2}, a V_{OC} of 2.03 V, and a FF of 82.5%. Simulated electrical parameters are close to the experimentally realized values provided in literatures [53–56]. The matched J_{SC} from optical and electrical simulations are very much comparable, which confirms the accuracy of our provided investigations. The proposed experimental realization of device fabrication is provided in the Methods Section. As a final step, investigated photovoltaic performance parameters are compared with the theoretical upper limit (SQ limit) of solar cells so that a better understanding of the performance of the solar

cell can be attained, which are demonstrated in Table 4. The SQ limits were calculated based on the original published paper by Shockley and Queisser in 1961 [13]. The SQ limit of J_{SC}, V_{OC}, *FF*, and ECE of the single-junction solar cells are provided in Fig. S14. It is observed that the investigated electrical parameters (V_{OC} and *FF*) are approaching ($\geq 90\%$) their theoretical limit, where J_{SC}s are ranging from 80–90% of its maximum value.

Nevertheless, it is assumed that the utilization of the potential surface and interface engineering can further amplify J_{SC}s. The ECE of investigated solar cells is continuing between 70 and 80% of its theoretical value. Hence, it is believed that the provided approach has a great potential to cross the SQ limit of the single-junction solar cells and will give a pathway to realize next-generation high-efficiency solar cells. In the case of PSCs, the front contact must be efficient to provide several advantages; hence, multi-layer systems are applied. In our case, SPD-grown TiO$_2$ by combined with other materials, act as the multi-layer front contact, which allows realizing high-efficiency single-junction PSCs and perovskite/perovskite TSCs. Moreover, the performance of PSCs can be further improved by exploiting efficient photonic structure, which improves the light trapping in PSCs [45, 57, 58]. Sanchez-Sobrado et al. demonstrated a low-cost light trapping structure based on TiO$_2$ and IZO materials by colloidal lithography (CL) process, which could be another potential strategy for realizing an improved photovoltaic efficiency [59, 60].

Table 3 Performance parameters for investigated perovskite single-junction and perovskite/perovskite tandem solar cells using FDTD optical simulation

Solar cell structure	Performance parameters						
	E_g (eV)	Max.GR (cm^{-3} s^{-1})	J_{SC} (mA cm^{-2})	V_{OC} (V)	FF (%)	P_{max} mW cm^{-2}	ECE (%)
Top PSC	1.6	1.2×10^{22}	23.6	1.15	83.5	22.661	22.7
Bottom PSC	1.16	2.1×10^{22}	34	0.89	80.5	24.356	24.4
2 T Perovskite/Perovskite TSC		1.0×10^{22}	18	2.03	82.5	30.156	30.2

Table 4 Comparison of the photovoltaic performance parameters of investigated perovskite single-junction and perovskite/perovskite tandem solar cells with theoretical upper limit or Shockley-Queisser (SQ) limit

Solar cell structure	Performance parameters				
	E_g (eV)	J_{SC} / J_{SC}^{SQ}	V_{OC}/V_{OC}^{SQ}	FF/FF^{SQ}	ECE/ECE^{SQ}
Top PSC	1.6	0.91	0.87	0.92	0.76
Bottom PSC	1.16	0.81	0.95	0.92	0.73
2 T Perovskite/Perovskite TSC		0.90	0.91	0.92	0.81

4 Summary

In this study, a multi-layer material system is investigated to prepare efficient front contact for perovskite single-junction and perovskite/perovskite tandem solar cells (TSCs). As a first step, a high-quality, reproducible, and scalable TiO_2 compact electron transport layer (ETL) has been prepared by spray pyrolysis deposition (SPD), which is a vital part of the front contact. The optimization of the compact TiO_2 has been extensively studied during the PSC fabrication. The optimized TiO_2 ETL has a thickness of 70 nm, which exhibits a J_{SC} of 21.3 mA cm^{-2}, V_{OC} of 1.07 V, *FF* of 72%, and ECE of 16.55%; up to our knowledge, this is so far the highest ECE achieved from a planar PSC with SPD-grown TiO_2 compact ETL. In this study, rigorous 3D optical-electrical coupled electromagnetic simulations have been used to study optics and electrical characteristics of solar cells, which allows us to validate findings from the experiments further. In the next step, we have proposed a multi-layer front contact design by combining with the optimized TiO_2 compact layer for efficient PSCs. The optimized single-junction device enhanced the ECE by 36%, with the improvement of J_{SC}, V_{OC}, *FF* by 10%, 7%, and 8.5%, respectively. Finally, the optimized device design has been advanced for the realization of efficient perovskite/perovskite TSCs. The PSO algorithm has carried the optimization of subcells in a tandem structure with 3D FDTD simulations. The proposed perovskite/perovskite TSC shows an ECE of ~30% under the matched short-circuit current condition. It is believed that such a realistic multi-layer front contact has excellent potential for the implementation of high-performance perovskite solar cells.

Electronic supplementary material The online version of this article (https://doi.org/10.1007/s40820-020-00559-2) contains supplementary material, which is available to authorised users.

References

1. S. Mahesh, J.M. Ball, R.D.J. Oliver, D.P. McMeekin, P.K. Nayak et al., Revealing the origin of voltage loss in mixed-halide perovskite solar cells. Energy Environ. Sci. **13**, 258 (2020). https://doi.org/10.1039/C9EE02162K

2. F. Gao, Y. Zhao, X. Zhang, J. You, Recent progresses on defect passivation toward efficient perovskite solar cells. Adv. Energy Mater. **10**, 1902650 (2020). https://doi.org/10.1002/aenm.201902650

3. A. Kojima, K. Teshima, Y. Shirai, T. Miyasaka, Organometal halide perovskites as visible-light sensitizers for photovoltaic cells. J. Am. Chem. Soc. **131**, 6050 (2009). https://doi.org/10.1021/ja809598r

4. N.-G. Park, Perovskite solar cells: an emerging photovoltaic technology. Mater. Today **18**, 65 (2015). https://doi.org/10.1016/j.mattod.2014.07.007

5. Y. Hou, E. Aydin, M. De Bastiani, C. Xiao, F.H. Isikgor et al., Pervasive functional translation of noncanonical human open reading frames. Science **367**, 1135 (2020). https://doi.org/10.1126/science.aay0262

6. NREL Transforming Energy (2020). https://www.nrel.gov/pv/cell-efficiency.html (accessed October 1, 2020)

7. D. Forgács, L. Gil-Escrig, D. Pérez-Del-Rey, C. Momblona, J. Werner et al., Efficient monolithic perovskite/perovskite tandem solar cells. Adv. Energy Mater. **7**, 1 (2017). https://doi.org/10.1002/aenm.201602121

8. R. Lin, K. Xiao, Z. Qin, Q. Han, C. Zhang et al., Monolithic all-perovskite tandem solar cells with 24.8% efficiency exploiting comproportionation to suppress Sn(II) oxidation in precursor ink. Nat. Energy **4**, 864 (2019)

9. M.I. Hossain, W. Qarony, V. Jovanov, Y.H. Tsang, D. Knipp, Nanophotonic design of perovskite/silicon tandem solar cells. J. Mater. Chem. A **6**, 3625 (2018). https://doi.org/10.1039/C8TA00628H

10. J. Werner, B. Niesen, C. Ballif, Perovskite/silicon tandem solar cells: marriage of convenience or true love story?–An overview. Adv. Mater. Interfaces **5**, 1700731 (2018). https://doi.org/10.1002/admi.201700731

11. M.I. Hossain, A.M. Saleque, S. Ahmed, I. Saidjafarzoda, M. Shahiduzzaman et al., Perovskite/perovskite planar tandem solar cells: A comprehensive guideline for reaching energy

conversion efficiency beyond 30%. Nano Energy **79**, 105400 (2021). https://doi.org/10.1016/j.nanoen.2020.105400

12. M.I. Hossain, W. Qarony, S. Ma, L. Zeng, D. Knipp, Y.H. Tsang, Perovskite/silicon tandem solar cells: from detailed balance limit calculations to photon management. Nano-Micro Lett. **11**, 58 (2019). https://doi.org/10.1007/s40820-019-0287-8

13. W. Shockley, H. Queisser, Detailed balance limit of efficiency of p-n junction solar cells. J. Appl. Phys. **32**, 510 (1961). https://doi.org/10.1063/1.1736034

14. A.K. Jena, A. Kulkarni, T. Miyasaka, Halide perovskite photovoltaics: background, status, and future prospects. Chem. Rev. **119**, 3036 (2019). https://doi.org/10.1021/acs.chemrev.8b00539

15. M.I. Hossain, A. Hongsingthong, W. Qarony, P. Sichanugrist, M. Konagai et al., Optics of perovskite solar cell front contacts. ACS Appl. Mater. Interface. **11**, 14693 (2019). https://doi.org/10.1021/acsami.8b16586

16. E.J. Juarez-Perez, M. Wußler, F. Fabregat-Santiago, K. Lakus-Wollny, E. Mankel et al., Role of the selective contacts in the performance of lead halide perovskite solar cells. J. Phys. Chem. Lett. **5**, 680 (2014). https://doi.org/10.1021/jz500059v

17. T. Moehl, J.H. Im, Y.H. Lee, K. Domanski, F. Giordano et al., Strong photocurrent amplification in perovskite solar cells with a porous TiO_2 blocking layer under reverse bias. J. Phys. Chem. Lett. **5**, 3931 (2014). https://doi.org/10.1021/jz502039k

18. M.I. Hossain, A. Mohammad, W. Qarony, S. Ilhom, D.R. Shukla et al., Atomic layer deposition of metal oxides for efficient perovskite single-junction and perovskite/silicon tandem solar cells. RSC Adv. **10**, 14856 (2020). https://doi.org/10.1039/D0RA00939C

19. M. Shahiduzzaman, S. Visal, M. Kuniyoshi, T. Kaneko, S. Umezu et al., Atomic layer deposition of metal oxides for efficient perovskite single-junction and perovskite/silicon tandem solar cells. Nano Lett. **19**, 598 (2019). https://doi.org/10.1021/acs.nanolett.8b04744

20. W. Qarony, M.I. Hossain, A. Salleo, D. Knipp, Y.H. Tsang, Rough versus planar interfaces: How to maximize the short circuit current of perovskite single and tandem solar cells. Mater. Today Energy **11**, 106 (2019). https://doi.org/10.1016/j.mtener.2018.10.001

21. M.I. Hossain, N. Yumnam, W. Qarony, A. Salleo, V. Wagner et al., Non-resonant metal-oxide metasurfaces for efficient perovskite solar cells. Sol. Energy **198**, 570 (2020). https://doi.org/10.1016/j.solener.2020.01.082

22. K. Mahmood, B.S. Swain, A.R. Kirmani, A. Amassian, Highly efficient perovskite solar cells based on a nanostructured WO_3–TiO_2 core–shell electron transporting material. J. Mater. Chem. A **3**, 9051 (2015). https://doi.org/10.1039/C4TA04883K

23. Y. Wu, X. Yang, H. Chen, K. Zhang, C. Qin et al., Highly compact TiO_2 layer for efficient hole-blocking in perovskite solar cells. Appl. Phys. Express **7**, 052301 (2014). https://doi.org/10.7567/APEX.7.052301

24. A. Möllmann, D. Gedamu, P. Vivo, R. Frohnhoven, D. Stadler et al., Highly compact TiO_2 films by spray pyrolysis and application in perovskite solar cells. Adv. Eng. Mater. **21**, 1801196 (2019). https://doi.org/10.1002/adem.201801196

25. S. Haque, M.J. Mendes, O. Sanchez-Sobrado, H. Águas, E. Fortunato et al., Photonic-structured TiO_2 for high-efficiency, flexible and stable perovskite solar cells. Nano Energy **59**, 91 (2019). https://doi.org/10.1016/j.nanoen.2019.02.023

26. M. Shahiduzzaman, H. Ashikawa, M. Kuniyoshi, S. Visal, S. Sakakibara et al., Compact TiO_2/Anatase TiO_2 single-crystalline nanoparticle electron-transport bilayer for efficient planar perovskite solar cells. ACS Sustain. Chem. Eng. **6**, 12070 (2018). https://doi.org/10.1021/acssuschemeng.8b02406

27. J.H. Noh, S.H. Im, J.H. Heo, T.N. Mandal, S. Il Seok, Chemical management for colorful, efficient, and stable inorganic–organic hybrid nanostructured solar cells. Nano Lett. **13**, 1764 (2013) https://doi.org/10.1021/nl400349b

28. A.K. Jena, H.-W. Chen, A. Kogo, Y. Sanehira, M. Ikegami et al., The interface between FTO and the TiO_2 compact layer can be one of the origins to hysteresis in planar heterojunction perovskite solar cells. ACS Appl. Mater. Interfaces **7**, 9817 (2015). https://doi.org/10.1021/acsami.5b01789

29. M.R. Leyden, L.K. Ono, S.R. Raga, Y. Kato, S. Wang et al., High performance perovskite solar cells by hybrid chemical vapor deposition. J. Mater. Chem. A **2**, 18742 (2014). https://doi.org/10.1039/C4TA04385E

30. C. Chen, Y. Cheng, Q. Dai, H. Song, Radio frequency magnetron sputtering deposition of TiO_2 thin films and their perovskite solar cell applications. Sci. Rep. **5**, 17684 (2016). https://doi.org/10.1038/srep17684

31. U. Schulz, R.W. Schaffer, Chapter 13-Optical coatings on plastic for antireflection purposes. in *Opt. Thin Film. Coatings* (Elsevier, 2018), pp. 517–537. https://doi.org/https://doi.org/10.1016/B978-0-08-102073-9.00013-8

32. A. Wakamiya, M. Endo, T. Sasamori, N. Tokitoh, Y. Ogomi et al., Colloidal-lithographed TiO_2 photonic nanostructures for solar cell light trapping. Chem. Lett. **43**, 711 (2014). https://doi.org/10.1246/cl.140074

33. M. Anaya, J.P. Correa-Baena, G. Lozano, M. Saliba, P. Anguita et al., Optical analysis of $CH_3NH_3Sn_xPb_{1−x}I_3$ absorbers: a roadmap for perovskite-on-perovskite tandem solar cells. J. Mater. Chem. A **4**, 11214 (2016). https://doi.org/10.1039/C6TA04840D

34. E. Raoult, R. Bodeux, S. Jutteau, S. Rives, A. Yaiche et al., Optical characterizations and modelling of semitransparent perovskite solar cells for tandem applications, 36th EU PVSEC 757 (2019). https://doi.org/https://doi.org/10.4229/EUPVSEC20192019-3BV.2.53

35. S. Sajid, A.M. Elseman, J. Ji, S. Dou, D. Wei et al., Computational study of ternary devices: stable, low-cost, and efficient planar perovskite solar cells. Nano-Micro Lett. **10**, 51 (2018). https://doi.org/10.1007/s40820-018-0205-5

36. S. Zandi, M. Razaghi, Finite element simulation of perovskite solar cell: A study on efficiency improvement based on structural and material modification. Sol. Energy **179**, 298 (2019). https://doi.org/10.1016/j.solener.2018.12.032

37. Y. Da, Y. Xuan, Q. Li, Quantifying energy losses in planar perovskite solar cells. Sol. Energy Mater. Sol. Cells **174**, 206 (2018). https://doi.org/10.1016/j.solmat.2017.09.002

38. P. Zhao, Z. Lin, J. Wang, M. Yue, J. Su et al., Numerical simulation of planar heterojunction perovskite solar cells based on SnO_2 electron transport layer. ACS Appl. Energy Mater. **2**, 4504 (2019). https://doi.org/10.1021/acsaem.9b00755

39. L.M. Herz, Charge-carrier mobilities in metal halide perovskites: fundamental mechanisms and limits. ACS Energy Lett. **2**, 1539 (2017). https://doi.org/10.1021/acsenergylett.7b00276

40. Q. Deng, Y. Li, L. Chen, S. Wang, G. Wang et al., The effects of electron and hole transport layer with the electrode work function on perovskite solar cells. Mod. Phys. Lett. B **30**, 1650341 (2016). https://doi.org/10.1142/S0217984916503413

41. M. Liu, M.B. Johnston, H.J. Snaith, Efficient planar heterojunction perovskite solar cells by vapour deposition. Nature **501**, 395 (2013). https://doi.org/10.1038/nature12509

42. M. Shahiduzzaman, S. Fukaya, E.Y. Muslih, L. Wang, M. Nakano et al., Metal oxide compact electron transport layer modification for efficient and stable perovskite solar cells. Materials **13**, 2207 (2020). https://doi.org/10.3390/ma13092207

43. A. Al Mamun, T.T. Ava, K. Zhang, H. Baumgart, G. Namkoong, New PCBM/carbon based electron transport layer for perovskite solar cells. Phys. Chem, **19**: 17960 (2017) https://doi.org/10.1039/C7CP02523H

44. M. Shahiduzzaman, A. Kulkarni, S. Visal, L. Wang, M. Nakano et al., A single-phase brookite TiO_2 nanoparticle bridge enhances the stability of perovskite solar cells. Sustain. Energy Fuels **4**, 2009 (2020). https://doi.org/10.1039/C9SE01133A

45. S. Haque, M. Alexandre, M.J. Mendes, H. Águas, E. Fortunato et al., Design of wave-optical structured substrates for ultrathin perovskite solar cells. Appl. Mater. Today **20**, 100720 (2020). https://doi.org/10.1016/j.apmt.2020.100720

46. R. Dewan, S. Fischer, V. Benno Meyer-Rochow, Y. Özdemir, S. Hamraz et al., Studying nanostructured nipple arrays of moth eye facets helps to design better thin film solar cells. Bioinspiration Biomimetics, **7**: 016003 (2012) https://doi.org/10.1088/1748-3182/7/1/016003

47. W. Qarony, M.I. Hossain, R. Dewan, S. Fischer, V.B. Meyer-Rochow et al., Approaching perfect light incoupling in perovskite and silicon thin film solar cells by moth eye surface textures. Adv. Theory Simulations **1**, 1800030 (2018). https://doi.org/10.1002/adts.201800030

48. F. Sahli, J. Werner, B.A. Kamino, M. Bräuninger, R. Monnard et al., Fully textured monolithic perovskite/silicon tandem solar cells with 252% power conversion efficiency. Nat. Mater, **17**: 820 (2018) https://doi.org/10.1038/s41563-018-0115-4

49. J. Im, C.C. Stoumpos, H. Jin, A.J. Freeman, M.G. Kanatzidis, Antagonism between spin–orbit coupling and steric effects causes anomalous band gap evolution in the perovskite photovoltaic materials $CH_3NH_3Sn_{1-x}Pb_xI_3$. J. Phys. Chem. Lett. **6**, 3503 (2015). https://doi.org/10.1021/acs.jpclett.5b01738

50. F. Hao, C.C. Stoumpos, P. Guo, N. Zhou, T.J. Marks et al., Solvent-mediated crystallization of $CH_3NH_3SnI_3$ films for heterojunction depleted perovskite solar cells. J. Am. Chem. Soc. **137**, 11445 (2015). https://doi.org/10.1021/jacs.5b06658

51. N.K. Noel, S.D. Stranks, A. Abate, C. Wehrenfennig, S. Guarnera et al., Lead-free organic–inorganic tin halide perovskites for photovoltaic applications. Energy Environ. Sci. **7**, 3061 (2014). https://doi.org/10.1039/c4ee01076k

52. A.K.M. Hasan, K. Sobayel, I. Raifuku, Y. Ishikawa, M. Shahiduzzaman et al., Optoelectronic properties of electron beam-deposited NiO_x thin films for solar cell application. Results Phys. **17**, 103122 (2020). https://doi.org/10.1016/j.rinp.2020.103122

53. A. Rajagopal, Z. Yang, S.B. Jo, I.L. Braly, P.-W. Liang et al., Highly efficient perovskite–perovskite tandem solar cells reaching 80% of the theoretical limit in photovoltage. Adv. Mater. **29**, 1702140 (2017). https://doi.org/10.1002/adma.201702140

54. D. Zhao, C. Chen, C. Wang, M.M. Junda, Z. Song et al., Efficient two-terminal all-perovskite tandem solar cells enabled by high-quality low-bandgap absorber layers. Nat. Energy **3**, 1093 (2018). https://doi.org/10.1038/s41560-018-0278-x

55. D.P. McMeekin, S. Mahesh, N.K. Noel, M.T. Klug, J. Lim et al., Solution-processed all-perovskite multi-junction solar cells. Joule **3**, 387 (2019). https://doi.org/10.1016/j.joule.2019.01.007

56. Y. Hu, L. Song, Y. Chen, W. Huang, Two-terminal perovskites tandem solar cells: recent advances and perspectives. Sol. RRL **3**, 1900080 (2019). https://doi.org/10.1002/solr.201900080

57. M.J. Mendes, S. Haque, O. Sanchez-Sobrado, A. Araújo, H. Águas et al., Optimal-enhanced solar cell ultra-thinning with broadband nanophotonic light capture. IScience **3**, 238 (2018). https://doi.org/10.1016/j.isci.2018.04.018

58. M. Alexandre, M. Chapa, S. Haque, M.J. Mendes, H. Águas et al., Optimum luminescent down-shifting properties for high efficiency and stable perovskite solar cells. ACS Appl. Energy Mater. **2**, 2930 (2019). https://doi.org/10.1021/acsaem.9b00271

59. O. Sanchez-Sobrado, M.J. Mendes, S. Haque, T. Mateus, H. Aguas et al., Lightwave trapping in thin film solar cells with improved photonic-structured front contacts. J. Mater. Chem. C **7**, 6456 (2019). https://doi.org/10.1039/C8TC06092D

60. O. Sanchez-Sobrado, M.J. Mendes, S. Haque, T. Mateus, A. Araujo et al., Colloidal-lithographed TiO_2 photonic nanostructures for solar cell light trapping. J. Mater. Chem. C **5**, 6852–6861 (2017). https://doi.org/10.1039/c7tc01756a